The open-loop control of MEMS: Modeling and experimental results

Katie M. Morzinski*[a,b], Kennet B. W. Harpsøe[a,b], Don T. Gavel[a,b], S. Mark Ammons[a,b]

[a] National Science Foundation Center for Adaptive Optics

[b] UCO/Lick Observatory and the Laboratory for Adaptive Optics, University of California, 1156 High St., Santa Cruz, CA 95064, USA

ABSTRACT

As adaptive optics (AO) technology progresses, both wide-field and high-order wavefront correction systems become reachable. Deformable mirrors (DMs) in these advanced architectures must exhibit exemplary performance to give low wavefront error. Such DMs must be economically attainable, meet stroke as well as flatness requirements, and show stable and repeatable actuation. Micro-electrical mechanical systems (MEMS) deformable mirrors, undergoing testing and characterization in the Laboratory for Adaptive Optics (LAO) at the University of California at Santa Cruz, show promise on these fronts. In addition to requiring advanced deformable mirror technology, these progressive AO architectures require advanced DM control algorithms. We therefore present a formulation for accurate open-loop control of MEMS deformable mirrors. The electrostatic actuators in a discrete-actuator MEMS device are attached via posts to a thin reflective top plate. The plate itself can be well-modeled by the thin plate equation. The actuators, although nonlinear in their response to applied voltage and deformation, are independent of each other except through forces transmitted by the top plate and can be empirically modeled via a calibration procedure we will describe. In this paper we present the modeling and laboratory results. So far in the lab we have achieved open loop control to ∼15 nm accuracy in response to arbitrary commands of ∼500 nm amplitude. Open-loop control enables a wealth of new applications for astronomical adaptive optics instruments, particularly in multi-object integral field spectroscopy, which we will describe.

Keywords: Open-loop control; MEMS; deformable mirrors; adaptive optics

1. INTRODUCTION

The advent of adaptive optics (AO) in astronomy has pioneered a new frontier of observation including resolution of Saturn's rings from Earth, discovery of brown dwarfs around nearby stars, massing of the compact object at our galaxy's center via stellar dynamics, and detection of galaxy merger remnants. Meanwhile, optometrists are using AO in vision science for retinal imaging to determine the origin of vision defects such as colorblindness. In imaging without applying AO, point sources are blurred not only by the diffraction limit but also by aberrations due to turbulence or other system imperfections. Employing AO compensates for the effects of such aberrations and hence enables these challenging observations to be made.

The main components of an AO system are the wavefront sensor, the control computer, and the deformable mirror (DM). The control computer takes input from the wavefront sensor and calculates what signal to send to the DM to create the desired phase. The DM then flattens the incoming wavefront by forming the given compensatory shape. Adaptive optics systems can be operated in either closed-loop or open-loop. In closed-loop, the wavefront sensor is located downstream of the deformable mirror and directly views, in real time, the effect of the DM correction on the wavefront. In open-loop, on the other hand, the wavefront sensor is blind to the deformable mirror and therefore requires a reliable, repeatable, well-modeled, and hence well-controlled DM.

*Contact: ktmorz@ucolick.org; tel +1 831 459-1949; fax +1 831 459-5265

1.1. Open-loop AO

The open-loop AO requirement of having a well-controlled DM has brought micro-electrical mechanical systems (MEMS) technology to the fore. Deformable mirrors consisting of MEMS actuators have been shown to provide stable and repeatable actuation at the sub-nanometer level.[1] Other benefits of MEMS DMs include their compact size, high actuator count, and accessible cost. This is in contrast to conventional piezo-electric DMs that must be operated in closed-loop due to hysteresis effects, and that are larger and more expensive per actuator than MEMS DMs. Furthermore, not only are MEMS DMs useful in open-loop AO, but using a well-modeled DM in closed-loop can reduce bandwidth error and even improve dual-mirror (i.e. "woofer/tweeter") algorithms by giving a known DM fit.

1.2. MEMS modeling for open-loop AO

In order to reap the benefits of utilizing a well-controlled MEMS DM, a model must be constructed of how the MEMS surface deforms with response to an input signal of voltages. The goal is to calculate the necessary voltage signal to send to the MEMS, given a desired DM surface shape. To achieve open-loop control, a DM model must be accurate and computationally fast. The residual error after applying the phase to the MEMS must be low because, with only a single iteration, the DM fitting error will include the residual from the DM shape application. The model must also be computationally inexpensive, to be done in real-time. This means the calculations must proceed in less than about 1 ms.

Previous work modeling MEMS DMs includes that done by T. Bifano et al. at Boston University who began with a numerical model using finite differencing[2] and who are now working with a primarily empirical model to achieve residual errors after one iteration of about 200 nm rms,[3] and C. Vogel et al. at Montana State University, who are working with a primarily mathematical model.[4] At the Laboratory for Adaptive Optics (LAO) at the University of California at Santa Cruz, we are also modeling our Boston Micromachines MEMS devices. Our model differs from the two noted above in that we combine mathematical modeling of the mirror surface with empirical measurements of the actuator forces to a high degree of accuracy. The MEMS model developed at the LAO has thus far reproduced arbitrary shapes of peak-valley amplitude $\sim$500 nm with residual errors of about 15 nm rms. In this paper the model is introduced, the calibration procedures are described, and the results of several open-loop trial runs are presented.

2. MEMS DEFORMABLE MIRRORS

At the LAO, MEMS devices received from Boston Micromachines Corporation are being characterized and tested for their performance in astronomical adaptive optics.[5] These MEMS studies are in support of next-generation AO technologies including extreme adaptive optics[6] (i.e. for the Gemini Planet Imager[7]) and multi-object adaptive optics[8] (i.e. for applications including the Thirty Meter Telescope[9]). The current status of Boston Micromachines MEMS development is presented in this volume.[10] One MEMS finding by the LAO is that MEMS actuators show sub-nanometer temporal stability as well as sub-nanometer position repeatability.[1] This result is promising for potential open-loop control of MEMS, as it is now known that MEMS actuators will precisely and faithfully go to a given input shape in voltage space. Now that precision has been proven, the next step is to achieve accuracy: to find a model to go from phase space to voltage space so that the voltage signal sent to the MEMS gives the correct phase.

In order to model Boston Micromachines MEMS deformable mirrors (pictured in Figure 1), we must understand their design. Figure 2 illustrates the structure of two actuators. Each pixel consists of a wired electrode at the bottom and a polysilicon actuator at the top. Polysilicon/oxide walls separate the pixels, and the actuator spring is connected via a polysilicon post to the mirror surface plate, which is also made of polysilicon and is coated in gold or aluminum. When a voltage is applied to the electrode, the actuator is attracted by the electrostatic force, pulling down the mirror surface at the post. When the voltage is released, the actuator spring provides the restoring force to return the mirror surface to its original position. Bifano et al. illustrate the structure of the Boston Micromachines actuator design in greater detail, in their second figure.[11]

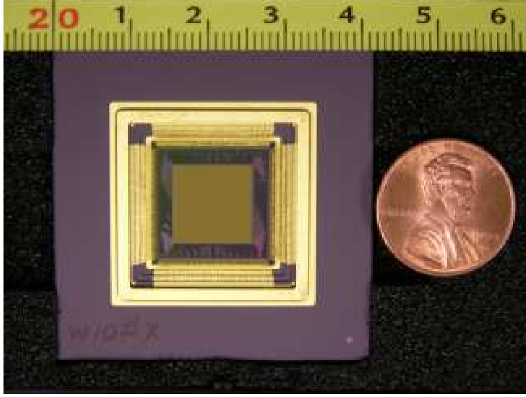

Figure 1. LAO photograph of a 1024-actuator Boston Micromachines MEMS deformable mirror. The actuators are arranged on a 32x32 square grid with 340 μm pitch. A U.S. penny and centimeter measuring tape are shown for scale.

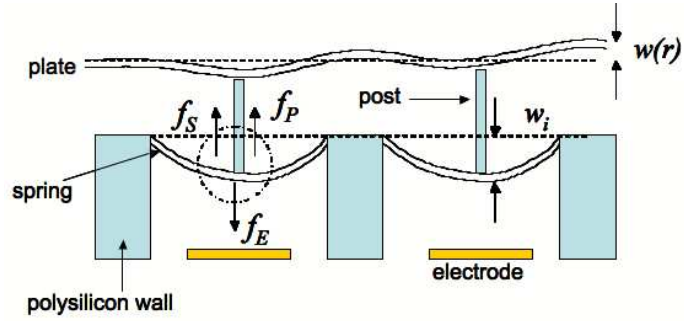

Figure 2. Forces and displacements in the MEMS deformable mirror. Two actuators are shown here, separated by polysilicon walls and connected to the mirror with rigid polysilicon posts. The mirror surface is 1 μm thick and is coated in a gold or aluminum layer on the order of 100 Å thick. Voltage is applied through wires bonded at the electrode. The plate force is given by the sum of the spring and electrostatic forces.

3. THE THIN PLATE EQUATION

The continuous facesheet of the MEMS is supported by a grid of actuators which in tandem deform the mirror surface to a wavefront-correcting shape. The actuators themselves will have nonlinear response characteristics with respect to applied voltages and their own internal displacements but are otherwise single-valued (i.e. non-hysteretic).

In this approach, taken by author K.B.W.H., we will only model the top surface mathematically. We assume that it can be modeled simply as a thin plate, in which case it deforms according to the plate equation:[12]

$$\nabla^4 w_z(r) = \frac{f_P(r)}{D}. \tag{1}$$

Note that we use the following assumptions for thin plates with small deflections taken from Timoshenko & Woinowsky-Krieger:[12]

1. There is no deformation in the middle plane of the plate. This plane remains *neutral* during bending.
2. Points of the plate lying initially on a normal-to-the-middle plane of the plate remain on the normal-to-the-middle surface of the plate after bending.
3. The normal stresses in the direction transverse to the plate can be disregarded.[12]

The quantities in the thin plate equation are: w_z = the displacement of the plate in the z-direction (i.e. perpendicular to the plane of the plate), $f_P(r)$ = the net force acting on the plate, and D = the flexural rigidity of the plate, given by

$$D = \frac{h^3 E}{12(1-\nu^2)}. \tag{2}$$

Here, h = the thickness of the plate, E = Young's modulus of elasticity, and ν = Poisson's ratio. The fourth derivative of the surface is given in Cartesian coordinates by

$$\nabla^4 w \equiv \frac{\partial^4 w}{\partial x^4} + 2\frac{\partial^4 w}{\partial x^2 \partial y^2} + \frac{\partial^4 w}{\partial y^4}. \tag{3}$$

3.1. Solution to the plate equation

We assume the only places forces can be exerted on the plate is through the springs, and assign $P =$ the point load on the plate. If we model a single actuator as a circular plate with clamped edges, loaded at the center, we convert to cylindrical coordinates:

$$\nabla^4 w(r) \equiv \frac{1}{r}\frac{d}{dr}\left\{r\frac{d}{dr}\left[\frac{1}{r}\frac{d}{dr}\left(r\frac{dw}{dr}\right)\right]\right\} \quad (4)$$

and write the solution to the plate equation as

$$w_z(r) = \frac{P}{16\pi D}\left[2r^2 \ln\frac{r}{a} - r^2 + a^2\right]. \quad (5)$$

The actuator spacing is given by a. Let the fundamental solution be defined as $\phi \equiv \left[2r^2 \ln\frac{r}{a} - r^2 + a^2\right]$ and let the coefficients which depend on the point load be defined as $c_{n,m} \equiv \frac{P}{16\pi D}$. We then write every solution to the top surface as a superposition of 1024 of these fundamental solutions on a grid of 32x32 actuators, in Cartesian coordinates:

$$w(x,y) = \sum_{n=1}^{N}\sum_{m=1}^{M} c_{n,m}\phi(x - x_n, y - y_m) \quad (6)$$

where $r = \sqrt{(x-x_n)^2 + (y-y_m)^2}$ and N and M are the number of actuators in the x and y directions.

3.2. Obtaining a matrix equation for the MEMS surface

We renumber the elements so that instead of a two-dimensional matrix of dimensions N by M, we have a one-dimensional matrix of dimensions $N \cdot M$. This allows us to write the solution as a single sum:

$$w(x,y) = \sum_{n=1}^{N\cdot M} c_n\phi(x - x_n, y - y_n). \quad (7)$$

If we discretize x and y to the same grid as the actuators, then this will be a matrix equation with $[\Phi]_{k,n} \equiv \phi(x_k - x_n, y_k - y_n)$:

$$w_k = c_n \cdot \Phi \quad (8)$$

and therefore, inverting the fundamental solution matrix Φ to obtain the forces c_n given the surface w_k, to get

$$c_n = w_k \cdot \Phi^{-1}. \quad (9)$$

Thus from a vector w_k of the displacements over each actuator and a simple matrix inverse Φ^{-1}, we can find the forces on the top surface. These forces are directly proportional to the coefficients c_n.

In the laboratory, a Zygo interferometer is used to measure the surface w_k. The matrix ϕ is found by poking one actuator and measuring its influence function. A simple inversion of matrix ϕ is determined using the IDL function *invert*. While this process is quite slow, it need only be done once and then the inverse of the matrix Φ^{-1} can be saved as an IDL variable to be restored when needed. The coefficients c_n, thus, are calculated as above, giving the forces on the plate. It remains, then, to separate the plate forces into the spring and electrostatic forces. The calibration procedures used to do this are described in the next section.

4. SEPARATING THE SPRING AND ELECTROSTATIC FORCES

In the previous section we went from the solution of the thin plate equation to the coefficients c_n, which are proportional to the forces. Now we must look at separating the forces on the plate f_P into the spring f_S and electrostatic f_E forces. The force balance in each actuator is given by

$$f_P(v,w) = f_S(w) + f_E(v,w) \quad (10)$$

where v denotes voltage and shows that the plate and electrostatic forces are a function of voltage v and displacement w, while the spring force is a function of displacement only.

4.1. Spring force

To first find the spring force alone, a calibration experiment is done in which a 3x3 array of actuators are initially set to 0 V. A Zygo interferometer was used to obtain the MEMS measurements. If voltage is applied to the outer actuators only, while the central actuator is left at 0 V, any subsequent displacement of the central actuator will be due to the spring force alone, as the central actuator's electrostatic force is known to be 0 when 0 V are applied:

$$f_S(w) = F_P(0, w) - f_E(0, w) = F_P(0, w). \tag{11}$$

Thus, the displacement of the central actuator is measured as the surrounding actuators are stepped down in voltage. Figure 3 illustrates, in an over-simplified and greatly exaggerated manner, this principle.

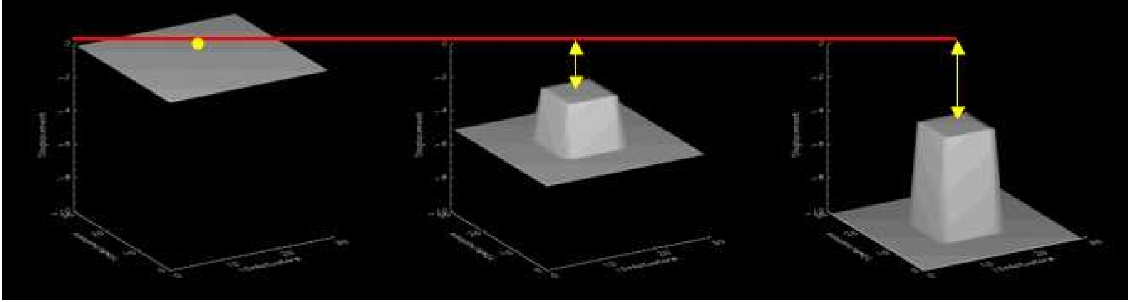

Figure 3. Simplified and exaggerated illustration of the principle behind spring-force calibration. A 3x3 array of actuators is tested. The central actuator is left at 0 V while the surrounding actuators are pulled down. Any displacement seen at the central actuator, therefore, is due to the spring force alone.

The actual experiment was done with the central actuator at 0 V and a rim of three actuators wide surrounding it set to varying voltages. The voltages of the surrounding actuators was stepped by increments of 5 V, from 0 V to 190 V. The measurements of the surface with the Zygo interferometer were then input into the previously described matrix method to derive the forces. As a result of this calibration procedure, the spring force on the central actuator could be plotted against displacement. Figure 4a plots the relation found. Thus the spring force has been obtained alone, separated from the electrostatic force.

4.2. Electrostatic force

The next step is to include the electrostatic force: the experiment was repeated, but with the variable of voltage on the central actuator also being changed. That is, the central actuator was set to one voltage and the rim of three actuators surrounding the central actuator was stepped in 5 V increments up to 190 V, and then the voltage on the central actuator was stepped up one increment and the surrounding actuators were again incremented up to 190 V. In this way all possible combinations of these two voltages were stepped through and measured with the Zygo interferometer. The forces were again obtained using the plate equation matrix method. Figure 4b shows the results of this calibration. Thus we obtained, through the above described methods, a matrix containing all of the physically realizable combinations of electrostatic force and spring force.

Note that in Figure 4b the z-axis "voltage on neighbors" shows remarkably little variation (and is hence compressed along that axis with the mean as the line and the range as the error bars in Figure 4c). This means that we found the electrostatic force to be largely independent of displacement. The electrostatic force seems, rather, to be only a function of the applied voltage on that particular actuator—the position of the neighbors has little effect. This was a surprising result, but one must note we have only tested one MEMS device so far. The facesheet of this particular device may have a stiffness such that the superposition of the influence functions from neighboring actuators is negligible. These calibration procedures would have to be run for other devices to determine the relative importance of the forces.

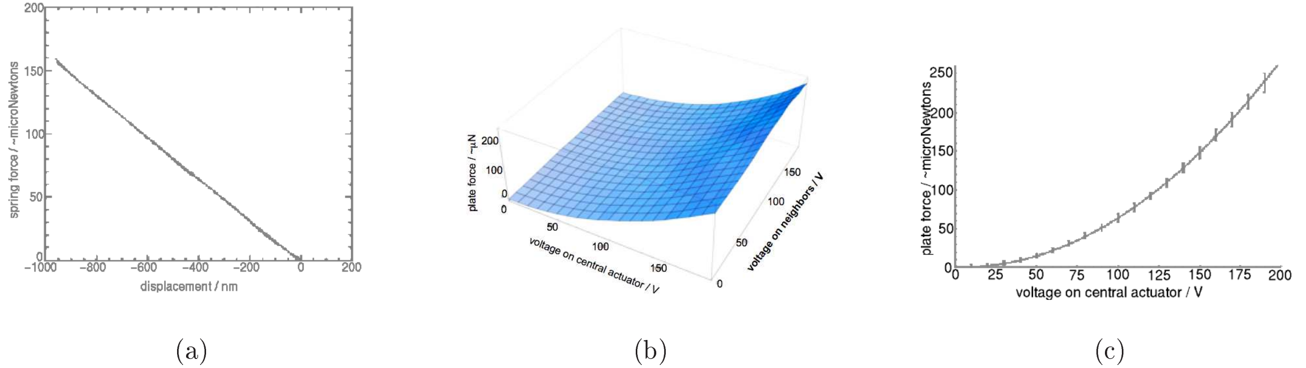

(a) (b) (c)

Figure 4. Resulting look-up tables from calibration procedure, for a representative actuator. (a) Plot of the spring force as a function of displacement for the central actuator. The force units are given as approximate μN because the flexural rigidity D of polysilicon is only determined to within 20%. The roughness of the units is insignificant as the forces are calibrated relative to the measurements. (b) Plot of the spring force (via voltage on neighbors as in Figure 4a) against plate force against voltage on central actuator. (c) If we compress Figure 4b along the z-axis ("voltage on neighbors") by taking the average and using the range as error bars, we get the figure shown here.

5. LABORATORY RESULTS OF OPEN-LOOP SHAPE APPLICATION

As our goal is to implement a successful open-loop MEMS model, we took the matrix solution to the plate equation combined with the displacement-to-voltage look-up tables created in the calibration process, and applied shapes to the MEMS using these tools. An arbitrary shape was created in phase space, the voltages were calculated using the look-up tables, and the result was applied to the MEMS. The Zygo interferometer was used to measure the shape, and then the residuals were found by comparing to the original desired shape. The comparison is not a trivial task as shifting, scaling, and rotation are introduced between the Zygo data and the IDL arrays.

5.1. Experimental data

We created a sinusoid of 600 nm peak-to-valley and wavelength 9 actuators and applied it to the MEMS. The measured sinusoid had a peak-to-valley of 550 nm and the residuals had a peak-to-valley of 85 nm and an rms of 16 nm. The results of this experiment are shown in Figure 5. While the residual error is satisfactorily low for an early run of the model, the structure in the residual image points to corrections that must be implemented in the code. Vertical features are likely reminiscent of shift error between the desired and measured sinusoids, while the darkest band at right reflects the systematic amplitude shortcoming of the model. The same experiment was repeated for a gaussian of input height 390 nm and FWHM 56 nm (see Figure 6). Finally, a Kolmogorov phase screen was applied to the MEMS (see Figure 7).

5.2. Discussion of results

The amplitude error reflected in Figures 5–7 is systematic and can be seen in greater detail by drawing a line-out through the desired and measured shapes. This is shown in Figure 8. To remedy this in the future, we are working on better calibration when aligning the Zygo data and the IDL arrays, and better shift and registration. Another source of this error could be compressing the three-dimensional look-up table (Figure 4b) into the two-dimensional look-up table of voltage on central actuator and plate force only (Figure 4c). Note that the error bars are greater at higher voltage. This will be investigated as a possible source of the amplitude systematics. We hope, with improvements to the code, to reduce the residual error and address the systematic effects.

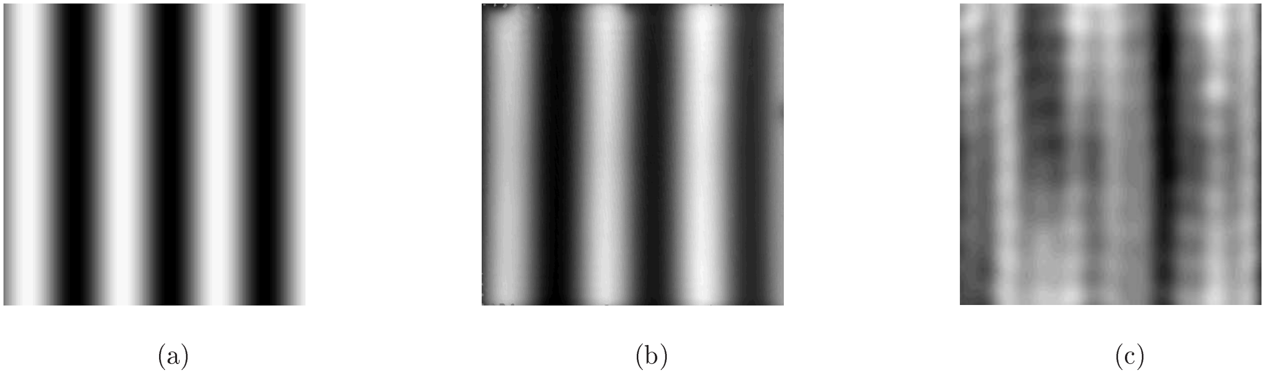

(a) (b) (c)

Figure 5. Open-loop experiment with sinusoid shape application. (a) Input sinusoid: peak-to-valley 600 nm. (b) Measured sinusoid: peak-to-valley 550 nm. (c) Residuals: peak-to-valley 85 nm and rms 16 nm.

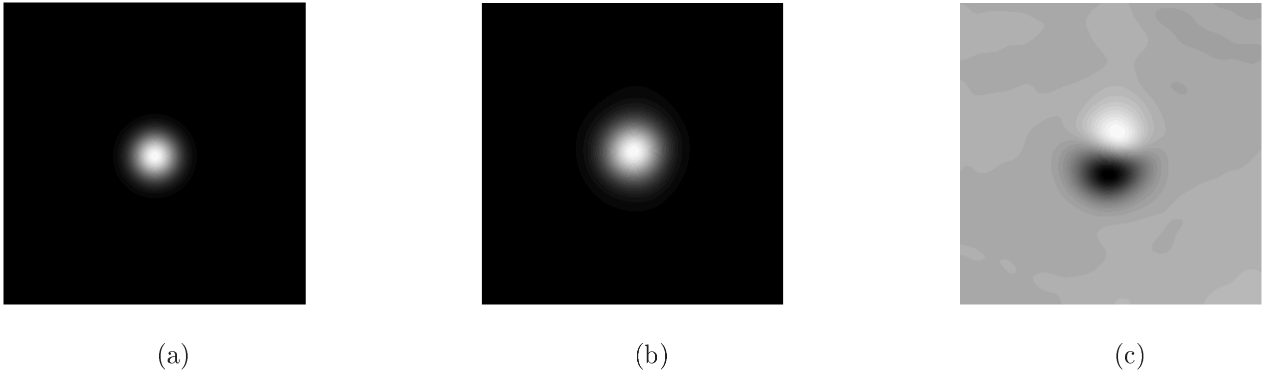

(a) (b) (c)

Figure 6. Open-loop experiment with gaussian shape application. (a) Input gaussian: peak-to-valley 390 nm and FWHM 56 nm. (b) Measured gaussian: peak-to-valley 370 nm. (c) Residuals: peak-to-valley 140 nm and rms 12 nm.

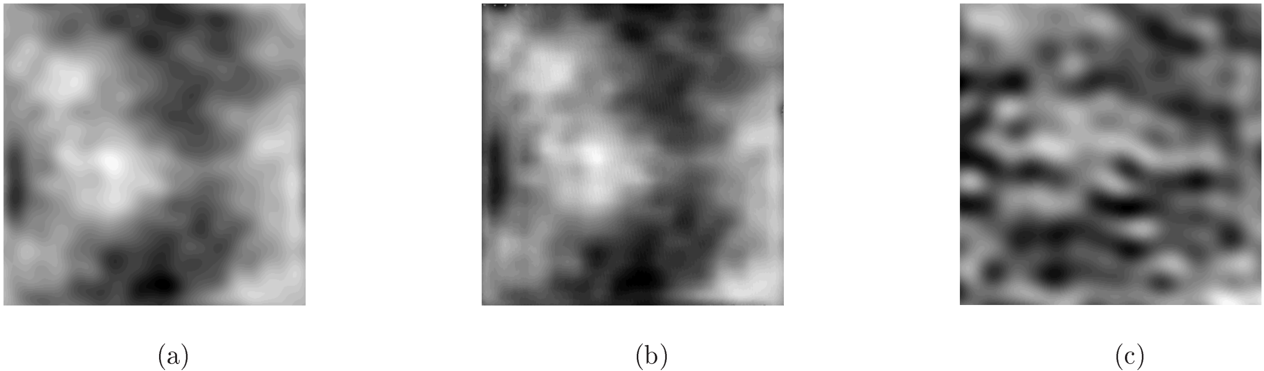

(a) (b) (c)

Figure 7. Open-loop experiment with Kolmogorov atmosphere shape application. (a) Input Kolmogorov: peak-to-valley 540 nm. (b) Measured Kolmogorov: peak-to-valley 480 nm. (c) Residuals: peak-to-valley 99 nm and rms 16 nm.

6. OTHER CONSIDERATIONS FOR OPEN-LOOP AO

6.1. Real-time control

The MEMS phase-to-voltage procedure described here is in its experimental stage in the LAO. Our open-loop method is fast because the real-time computations involved are simple look-up table processes. Each actuator

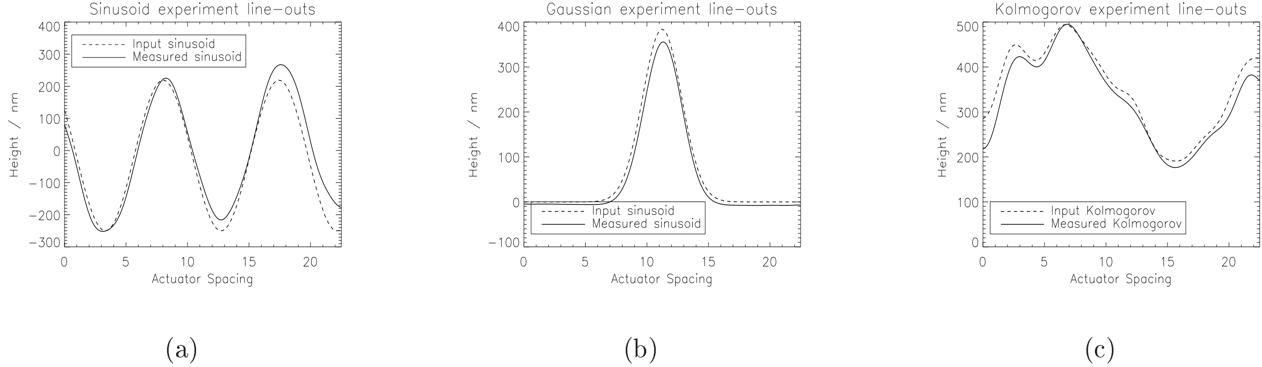

Figure 8. Comparison of line-outs for each open-loop shape application experiment. Dashed line: desired shape. Solid line: measured shape. (a) Sinusoid experiment. (b) Gaussian experiment. (c) Kolmogorov experiment.

look-up is independent of every other, so the method would benefit greatly from parallelization. There are three look-ups per actuator, and one look-up generally takes about one "flop." Thus, on a dedicated processor, we expect to be able to use this method in real-time.

6.2. Wavefront sensing

Open-loop wavefront sensing is nontrivial as extensive linearity calibrations are required to report wavefront slopes over a large dynamic range with high accuracy. Author S.M.A. is actively involved in pursuing this aspect of open-loop control on the multi-object adaptive optics (MOAO) testbed in the LAO. This work coupled with the MEMS modeling work will enable the LAO team to assemble a full open-loop AO correction system in the near future.

7. ON-SKY TESTING

The open-loop MEMS control method described in this paper will be tested on-sky in this year. We are developing a prototype AO system for the 1-meter Nickel telescope at Lick Observatory. This project is called ViLLaGeS (Visible Light Laser Guide Star System) and author D.T.G. is the Principal Investigator. ViLLaGeS will be a visible-light MEMS-based AO system. Key technologies to be tested on-sky include MEMS performance, open-loop MEMS control, and laser uplink. Lick Observatory has a strong history of initiating progressive AO technologies, such as the AO system developed for the 3-meter Shane telescope.[13] With ViLLaGeS we will continue that tradition to path-find for future advanced wavefront-correction instruments.

8. APPLICATIONS FOR OPEN-LOOP MEMS CONTROL

There are many possible applications for open-loop adaptive optics. Example systems that may require open-loop control are any scheme where the signal is too low to split the beam or where the correction is needed too rarely to warrant the complexity of a second path. MEMS deformable mirrors can provide the solution to these myriad advanced wavefront-correction problems.

Having a well-understood DM model can also benefit traditional closed-loop AO systems because faster closing of the loop can potentially reduce bandwidth error. Additionally, several dual-mirror AO systems are being developed with a high-stroke "woofer" DM to remove the low-frequency aberrations and a lower-stroke but higher-actuator-count "tweeter" DM to remove the high-frequency aberrations.[14] These woofer/tweeter systems will also benefit from a well-understood DM model, as cross-talk errors may be addressed if at least one of the DMs behaves in a well-modeled fashion.

One open-loop application is multi-object adaptive optics (MOAO). The IRMOS near-infrared multi-object spectrograph for the Thirty Meter Telescope is considered with a MOAO system.[15] In this design, a constellation of laser guide stars will illuminate the atmosphere above the telescope, with a wavefront sensor for each guide star. Tomography will be used to reconstruct the three-dimensional phase volume. Meanwhile, an array of

science targets will each be assigned a DM. Each DM will give the best correction along its science target's line-of-sight, based on the tomographic reconstruction of that path. Because the science objects are faint and the target-photon paths differ from the laser-photon wavefront sensing paths, the process will be photon-starved and complex. Thus open-loop control is necessary for simplicity and signal-to-noise reasons. Through the LAO team's work on MEMS modeling and wavefront sensing,[8] MOAO is a promising architecture.

Open-loop control is also alluring for space missions such as the Terrestrial Planet Finder. Because wavefront correction in space is needed infrequently (i.e. to adjust for thermal distortions), simplicity in optical design can be retained. Thus, focal-plane imaging algorithms have been proposed[16] for wavefront sensing, rather than an alternate optical path. A well-modeled DM, then, would provide significant benefit in this arena as well.

9. CONCLUSIONS

We have presented a model for accurate open-loop control of MEMS deformable mirrors. The thin plate equation is used to model the surface, and the forces are calibrated once and then inserted into look-up tables. Thus, a computationally efficient phase-to-voltage algorithm is used to apply shapes to the MEMS DM. In laboratory experiments at the LAO, open-loop application was found to be accurate to $\sim$15 nm rms given input shapes of 500 nm amplitude. As precision was proven earlier[1] and now accuracy has been addressed in this paper, significant progress has been made towards real-time open-loop control of MEMS DMs. Potential applications for this work include multi-object adaptive optics, space-based wavefront correcting, woofer/tweeter algorithms, and traditional closed-loop AO in some cases. After improvements to the code, the method will be tested on-sky at Lick Observatory this year as part of the ViLLaGeS MEMS-based AO project.

ACKNOWLEDGMENTS

We thank Marco Reinig of the LAO team, who crafted the communication code between the Zygo and IDL, and assisted with other programming matters. We thank Daren Dillon of the LAO team, who prepared the Zygo interferometer for the MEMS measurements, and trouble-shot the data-taking process.

Jerry Nelson is acknowledged for an insightful discussion posing the idea of separating the plate equation from actuator dynamics. Boston Micromachines Corporation and Tom Bifano provided useful discussions and data about their MEMS devices. David L. Windt of Columbia University kindly emailed the IDL procedure used to read Zygo data, which can also be found integrated into his TOPO package of IDL routines for surface topography analysis.

This research was supported in part by the National Science Foundation Science and Technology Center for Adaptive Optics, managed by the University of California at Santa Cruz under cooperative agreement No. AST-9876783, and directed by Claire E. Max. Support for this work was also provided by a grant from the Gordon and Betty Moore Foundation to the Regents of the University of California, Santa Cruz, on behalf of the UCO/Lick Laboratory for Adaptive Optics. The content of the information does not necessarily reflect the position or the policy of the Gordon and Betty Moore Foundation, and no official endorsement should be inferred.

REFERENCES

1. K. M. Morzinski, J. W. Evans, S. Severson, B. Macintosh, D. Dillon, D. Gavel, C. Max, and D. Palmer, "Characterizing the potential of MEMS deformable mirrors for astronomical adaptive optics," in *Advances in Adaptive Optics II*, B. L. Ellerbroek and D. B. Calia, eds., *Proc. SPIE* **6272**, p. 627221, 2006.
2. T. G. Bifano, R. K. Mali, J. K. Dorton, J. Perreault, N. Vandelli, M. N. Horenstein, and D. A. Castañon, "Continuous-membrane surface-micromachined silicon deformable mirror," *Opt. Eng.* **36 No.5**, pp. 1354–1360, 1997.
3. Y. Zhou and T. Bifano, "Adaptive optics using a MEMS deformable mirror," in *5th International Workshop on Adaptive Optics for Industry and Medicine*, W. Jiang, ed., *Proc. SPIE* **6018**, p. 601817, 2005.
4. C. R. Vogel and Q. Yang, "Modeling, simulation, and open-loop control of a continuous facesheet MEMS deformable mirror," *JOSA A* **23**, pp. 1074–1081, 2006.

5. D. Gavel, "MEMS development for astronomical instrumentation at the Lick Observatory Laboratory for Adaptive Optics," in *MEMS Adaptive Optics*, S. S. Olivier, T. G. Bifano, and J. A. Kubby, eds., *Proc. SPIE* **6467**, p. this meeting, 2007.
6. S. A. Severson, B. Bauman, D. Dillon, J. Evans, D. Gavel, B. Macintosh, K. Morzinski, D. Palmer, and L. Poyneer, "The Extreme Adaptive Optics Testbed at UCSC: Current results and coronagraphic upgrade," in *Advances in Adaptive Optics II*, B. L. Ellerbroek and D. B. Calia, eds., *Proc. SPIE* **6272**, p. 62722J, 2006.
7. B. Macintosh, J. Graham, D. Palmer, R. Doyon, D. Gavel, J. Larkin, B. Oppenheimer, L. Saddlemyer, J. K. Wallace, B. Bauman, J. Evans, D. Erikson, K. Morzinski, D. Phillion, L. Poyneer, A. Sivaramakrishnan, R. Soummer, S. Thibault, and J.-P. Veran, "The Gemini Planet Imager," in *Advances in Adaptive Optics II*, B. L. Ellerbroek and D. B. Calia, eds., *Proc. SPIE* **6272**, p. 62720L, 2006.
8. S. M. Ammons, R. Kupke, E. A. Laag, D. T. Gavel, D. R. Dillon, M. R. Reinig, B. J. Bauman, C. E. Max, and J. A. Johnson, "First results from the UCSC Laboratory for Adaptive Optics multi-conjugate and multi-object adaptive optics testbed," in *Advances in Adaptive Optics II*, B. L. Ellerbroek and D. B. Calia, eds., *Proc. SPIE* **6272**, p. 627202, 2006.
9. B. L. Ellerbroek, C. Boyer, C. Bradley, M. C. Britton, S. Browne, R. A. Buchroeder, J.-L. Carel, M. K. Cho, M. R. Chun, R. Clare, R. Conan, L. G. Daggert, R. G. Dekany, J. H. Elias, D. A. Erickson, R. Flicker, D. T. Gavel, L. Gilles, P. Hampton, G. Herriot, M. R. Hunten, R. R. Joyce, M. Liang, B. A. Macintosh, R. Palomo, I. P. Powell, S. C. Roberts, E. Ruch, J.-C. Sinquin, M. J. Smith, J. A. Stoesz, M. Troy, G. A. Tyler, J.-P. Veran, C. R. Vogel, and Q. Yang, "A conceptual design for the Thirty Meter Telescope adaptive optics system," in *Advances in Adaptive Optics II*, B. L. Ellerbroek and D. B. Calia, eds., *Proc. SPIE* **6272**, p. 62720D, 2006.
10. P. A. Bierden, "Recent advances in MEMS deformable mirror technology," in *MEMS Adaptive Optics*, S. S. Olivier, T. G. Bifano, and J. A. Kubby, eds., *Proc. SPIE* **6467**, p. this meeting, 2007.
11. T. Bifano, P. Bierden, and J. Perreault, "Micromachined deformable mirrors for dynamic wavefront control," in *Advanced Wavefront Control: Methods, Devices and Applications II*, J. D. Gonglewski, M. T. Gruineisen, and M. K. Giles, eds., *Proc. SPIE* **5553**, pp. 1–16, 2004.
12. S. Timoshenko and S. Woinowsky-Krieger, *Theory of plates and shells*, McGraw-Hill Book Company, Inc., New York, 1959 (second edition).
13. S. S. Olivier, J. R. An, K. Avicola, H. D. Bissinger, J. M. Brase, H. W. Friedman, D. T. Gavel, E. M. Johansson, C. E. Max, K. E. Waltjen, W. A. Fisher, and W. C. Bradford, "Performance of adaptive optics at Lick Observatory," in *Adaptive Optics in Astronomy*, M. A. Ealey and F. Merkle, eds., *Proc. SPIE* **2201**, p. 1110, 1994.
14. P. J. Hampton, R. Conan, C. Bradley, and P. Agathoklis, "Control of a woofer tweeter system of deformable mirrors," in *Advanced Software and Control for Astronomy*, H. Lewis and A. Bridger, eds., *Proc. SPIE* **6274**, p. 62741Z, 2006.
15. D. R. Andersen, S. S. Eikenberry, M. Fletcher, W. Gardhouse, B. Leckie, J.-P. Veran, D. Gavel, R. Clare, R. Guzman, L. Jolissaint, R. Julian, and W. Rambold, "The MOAO system of the IRMOS near-infrared multi-object spectrograph for TMT," in *Ground-based and Airborne Instrumentation for Astronomy*, I. S. McLean and M. Iye, eds., *Proc. SPIE* **6269**, p. 62694K, 2006.
16. P. J. Bordé and W. A. Traub, "High-contrast imaging from space: Speckle nulling in a low-aberration regime," *ApJ* **638 No.1**, pp. 488–498, 2006.